5

MULTI-SPHERE UNIT CELL MODEL

5.1 INTRODUCTION

Chapter 3 presented a detailed description of various correlations used to simulate the effective thermal conductivity k_{eff}. It demonstrated that much empiricism is incorporated into the various models to achieve the desired simulation results in the prediction of the effective thermal conductivity.

The focus of this chapter is the development of a new model for the effective conductivity that includes the following seven heat transfer mechanisms: (1) conduction through the solid; (2) conduction through the contact area between spheres while incorporating surface roughness; (3) conduction through the gas phase; (4) thermal radiation between solid surfaces; (5) conduction between spheres and the wall interface; (6) conduction through the gas phase in the wall region; and (7) thermal radiation between spheres and the wall interface.

Bahrami *et al.* (2006:3691) attempted to use fundamental heat transfer principals to characterise heat transfer mechanisms between two connecting rough solid bodies. Their model only addressed conduction through the contact area between spheres while incorporating surface roughness and conduction through the gas phase at lower temperatures. Good results were obtained when comparing the model with SC packing experimental results. However, simulation results deviated slightly when it was compared with a FCC packing. No attempt was made to compare the model with the results from a randomly packed bed due to the inadequate provision to implement structural variation into their model. Therefore, it can be concluded that the model proposed by Bahrami *et al.* (2006:3691) is not necessarily applicable to randomly packed beds in PBRs, as they only address structured packings and disregard any contribution of thermal radiation.

The new model developed in this chapter will however be based on some of the thermal conduction heat transfer principles used by Bahrami *et al.* (2006:3691). The newly developed

Multi-sphere Unit Cell Model addresses all the aforementioned heat transfer mechanisms, while distinguishing between short range thermal radiation, defined as radiation to and from spheres in contact with the sphere under consideration and long range thermal radiation, defined as radiation to and from spheres not in direct contact with the sphere under consideration.

5.2 DEVELOPMENT OF THE MULTI-SPHERE UNIT CELL MODEL

For the bulk and near-wall regions of a randomly packed bed the Multi-sphere Unit Cell model consists of two primary components:

$$k_{eff} = k_e^{g,c} + k_e^r \tag{5.1}$$

where the thermal conductivity $k_e^{g,c}$ incorporates conduction through the solid, conduction through the contact area between spheres while incorporating surface roughness and conduction through the gas phase, while the radiative thermal conductivity k_e^r, addresses the thermal radiation between solid surfaces (short-range and long-range). In the wall region, i.e. for spheres with centre points a distance of $0.5d_p$ from the wall interface, the model consists of two components, which is given by:

$$k_{eff}^W = k_e^{g,c,W} + k_e^{r,W} \tag{5.2}$$

where $k_e^{g,c,W}$ incorporates conduction between spheres and the wall interface as well as conduction through the gas phase in the wall region, while $k_e^{r,W}$ is the thermal radiation from the pebble in contact with the wall interface (short-range), as well as pebble further away radiating through voids (long-range).

5.1.1 CONDUCTION

The first parameter to address is that of thermal conduction in the bulk region of the packed bed namely $k_e^{g,c}$. The Multi-sphere Unit Cell Model is based on two half spheres divided into three radial regions, namely the inner, middle and outer regions. Unlike other models presented in Chapter 3, that mainly used a lumping of empirical correlations to characterise the thermal conduction, the Multi-sphere Unit Cell Model treats each heat transfer mechanism as unique in a specific region of the unit cell and represent each heat transfer mechanism as a thermal resistance. This is also different to the Bahrami *et al.* (2006:3691) model who discards solid conduction and who is limited to structured packings.

In the Multi-sphere Unit Cell model each of these regions consists of an arrangement of series and parallel resistances, as demonstrated in Figure 5.1. Two thermal resistance networks are developed to calculate the combined joint thermal resistance between two half spheres R_j, i.e. the rough contact network and the Hertzian contact network. The rough contact network is used to simulate hard spheres with rough surfaces of a Brinell hardness of $1.3 \leq H_B \leq 7.6GPa$ or a Brinell Hardness Number (BHN) of $133 \leq BHN \leq 775$, whereas the Hertzian contact network is used for $H_B < 1.3GPa$ or where the need is not identified to simulate $k_e^{g,c}$ in such detail.

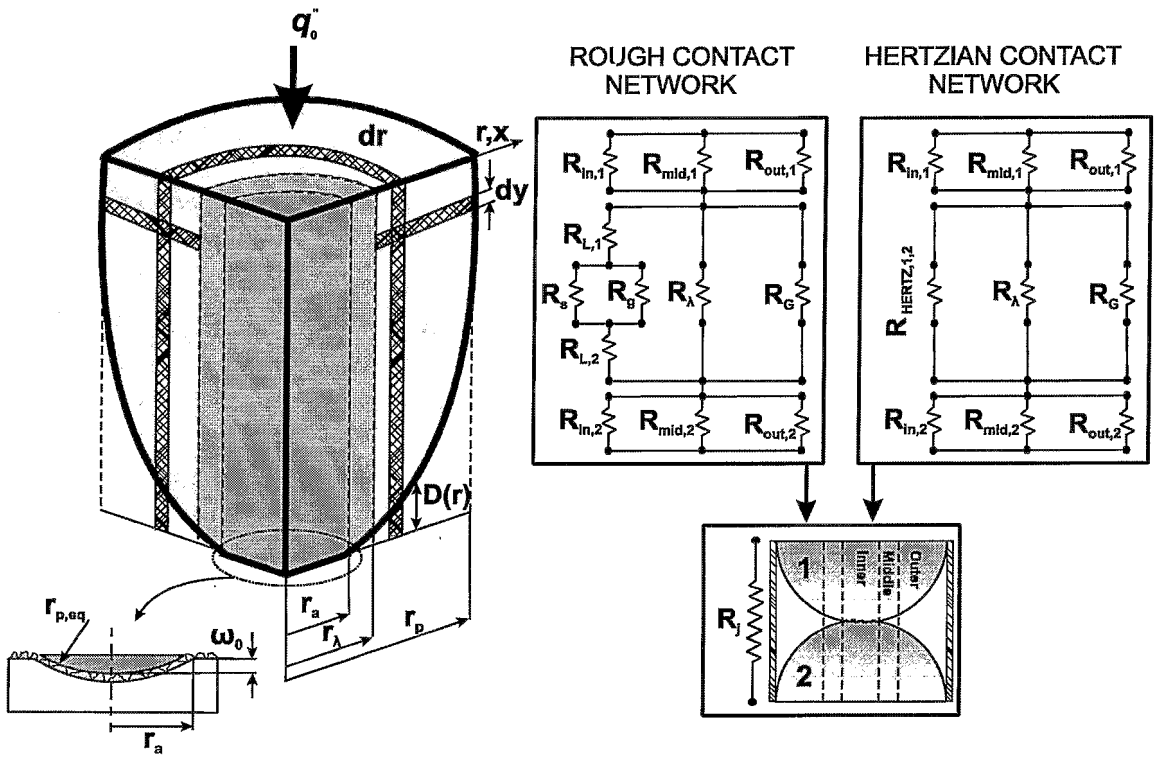

Figure 5.1: Multi-sphere Unit Cell Model (conduction)

The rough contact network consists of eight thermal resistance components: (1) the inner solid material resistance $R_{in,1,2}$ (summation of $R_{in,1}$ and $R_{in,2}$); (2) the macrocontact constriction/spreading resistance $R_{L,1,2}$ developed by Bahrami *et al.* (2006:3691), (summation of $R_{L,1}$ and $R_{L,2}$) ; (3) the microcontact constriction/spreading resistance R_s developed by Bahrami *et al.* (2006:3691); (4) the resistance of the interstitial gas in the microgap R_g developed by Bahrami *et al.* (2006:3691); (5) the middle solid material resistance $R_{mid,1,2}$ (summation of $R_{mid,1}$ and $R_{mid,2}$); (6) the resistance of the interstitial gas in the Knudsen regime (Smoluchowski effect) of the macrogap R_λ; (7) the outer solid material resistance $R_{out,1,2}$ (summation of $R_{out,1}$ and $R_{out,2}$); and (8) the resistance of the interstitial gas in the

macrogap R_G. In the Hertzian network, $R_{L,1,2}$, R_s and R_g is replaced by the Hertzian microcontact $R_{HERTZ,1,2}$ developed by Chen & Tien (1973:302). The Herzian network in essence discards surface roughness and treats solid surfaces as smooth.

Finally, the Multi-sphere Unit Cell Model combines the joint thermal resistances in a unique manner between two half spheres. It is unique in the sense that it divides the effective thermal conductivity between two spheres into three regions i.e. inner, middle and outer. Each of these regions addresses specific heat transfer mechanisms which is summand to give the joint thermal resistance R_j. It further assumes that sphere one and sphere two consist of the same material, which entails that the solid material thermal resistances in a specific region can be summed. For example the summation of the inner solid material resistance $R_{in,1}$ and $R_{in,2}$ is denoted as $R_{in,1,2}$. The joint thermal resistance for the rough contact network can therefore be calculated as follows:

$$\begin{aligned} R_j &= \left(\frac{1}{R_{in,1}}+\frac{1}{R_{mid,1}}+\frac{1}{R_{out,1}}\right)^{-1}+\left(\frac{1}{R_{L,1,2}+\left(\frac{1}{R_g}+\frac{1}{R_s}\right)^{-1}}+\frac{1}{R_\lambda}+\frac{1}{R_G}\right)^{-1} \\ &\quad +\left(\frac{1}{R_{in,2}}+\frac{1}{R_{mid,2}}+\frac{1}{R_{out,2}}\right)^{-1} \\ &= \left(\frac{1}{R_{L,1,2}+\left(\frac{1}{R_g}+\frac{1}{R_s}\right)^{-1}}+\frac{1}{R_\lambda}+\frac{1}{R_G}\right)^{-1}+2\left(\frac{1}{R_{in}}+\frac{1}{R_{mid}}+\frac{1}{R_{out}}\right)^{-1} \\ &= \left(\frac{1}{R_{L,1,2}+\left(\frac{1}{R_g}+\frac{1}{R_s}\right)^{-1}}+\frac{1}{R_\lambda}+\frac{1}{R_G}\right)^{-1}+\left(\frac{1}{R_{in,1,2}}+\frac{1}{R_{mid,1,2}}+\frac{1}{R_{out,1,2}}\right)^{-1} \end{aligned} \tag{5.3}$$

The combined joint thermal resistance between two half spheres for the Hertzian contact network can be calculated as follows:

$$R_j = \left(\frac{1}{R_{HERTZ,1,2}}+\frac{1}{R_\lambda}+\frac{1}{R_G}\right)^{-1}+\left(\frac{1}{R_{in,1,2}}+\frac{1}{R_{mid,1,2}}+\frac{1}{R_{out,1,2}}\right)^{-1} \tag{5.4}$$

INNER REGION CONDUCTION:

For the rough contact network in the inner region, the thermal contact resistances developed by Bahrami *et al.* (2006:3691) were used, that is the micro- and macrocontact thermal resistances R_s and $R_{L,1,2}$, as well as the interstitial gas resistance R_g in the microgap. The full explanation of these thermal resistances was given in Section 3.2.2. However, for completeness sake, these thermal resistances are explained briefly again below.

Bahrami *et al.* (2006:3691) assumed that all surfaces are Gaussian, with Gaussian defined as isotropic and randomly rough. Microcontacts occur when randomly rough surfaces are placed under a mechanical load, where the real contact area A_m (the summation of the microcontacts) forms a small portion of the nominal contact area.

The compact model to predict the thermal resistance through the microcontacts R_s, assuming plastically deformed asperities, is given by:

$$R_s = \frac{0.565H^*\left(\frac{\sigma_{RMS}}{m_{RMS}}\right)}{k_s F} \tag{5.5}$$

where k_s, H^*, σ_{RMS}, m_{RMS} can be obtained in Eq. (3.106) to Eq. (3.108) and Eq. (3.111), respectively. The macrocontact thermal resistance, which simulates the contact pressure distribution on the isothermal contact area, is given by:

$$R_{L,1,2} = \frac{1}{2k_s r_a} \tag{5.6}$$

where r_a is calculated by Eq. (3.113). Note that the contact area radius is renamed in the Multi-sphere Unit Cell Model as $r_a = a_L$. The microgap interstitial gas resistance for the contact of two rough spheres can be calculated by:

$$R_g = \frac{2\sqrt{2}\sigma_{RMS}a_2}{\pi k_g r_a^2 \ln\left(1+\frac{a_2}{a_1+\left(j/2\sqrt{2}\sigma_{RMS}\right)}\right)} \tag{5.7}$$

where a_1 and a_2 are parameters that can be obtained from Eq. (3.124) and j is the temperature jump parameter that can be obtained from Eq. (3.120). The molecular mean free-path λ which is one of the parameters of j is defined as the average distance a gas molecule travels before colliding with another gas molecule and is proportional to the gas

temperature and inversely proportional to the gas pressure as previously mentioned $\lambda = \left(P_0 T_g / P_g T_0\right)\lambda_0$ (Kennard, 1938:311).

For the Hertzian contact network the macrocontact thermal resistance changes to $R_{HERTZ,1,2}$. The macrocontact thermal resistance that uses the Hertzian contact radius r_c defined in Eq. (3.101) and developed by Chen & Tien (1973:302) is given by:

$$R_{HERTZ,1,2} = \frac{0.64}{k_s r_c} \tag{5.8}$$

It must be emphasised that when using the Hertzian thermal resistance network, the material deformation depth correlation changes to:

$$\omega_0 = \frac{r_c^2}{2r_p} \tag{5.9}$$

The fuel matrix of the solid material in a PBR has various thermal conductivities in various zones. It is therefore important to develop thermal resistance models to calculate the heat transfer through such a solid section. In this study, it is assumed that the solid material is isothermal with the same thermal conductance in the solid region under consideration. It is important to note that $R_{in,1,2}$ can be broken up in other thermal resistances acting in series, in order to incorporate the different thermal conductivity regions in a pebble fuel matrix. Nonetheless, by assuming one-dimensional heat conduction through the bulk solid material in the inner region, the heat flux can be defined as:

$$Q = \frac{kA_c}{L}\left(T_1 - T_2\right) \tag{5.10}$$

where the thermal resistance is:

$$R = \frac{L}{kA_c} \tag{5.11}$$

In incorporating the material deformation depth $\omega_0 = r_a^2 / 2r_{p,eq}$ defined by Bahrami *et al.* (2006:3691), into the effective length L with the conduction area $A_c = \pi r_a^2$, a thermal resistance for the inner solid region in the rough contact network can be defined by considering an isothermal boundary plane for both spheres. This is given by:

$$R_{in,1,2} = 2\frac{\left(r_p - \omega_0/2\right)}{k_s \pi r_a^2} = \frac{\left(d_p - \omega_0\right)}{k_s \pi r_a^2} \tag{5.12}$$

where k_s is the thermal conductivity of the solid material, d_p is the sphere diameter and r_a is

the contact area radius calculated by Eq. (3.113). It is important to note that the equivalent pebble radius $r_{p,eq} = r_p/2$, for this setup, which is obtained from Eq. (3.116). However, further investigation regarding quantification of the equivalent pebble radius is done in Chapter 6.

For the Hertzian contact network, $R_{in,1,2}$ is defined in the same manner as displayed in Eq. (5.12), with the exception of r_a changing to r_c which can be calculated with Eq. (3.101).

MIDDLE REGION CONDUCTION:

Conduction heat transfer through a gas layer between two planes can be grouped into multiple categories, as illustrated in Figure 3.2. Yovanovich (1982:83) proposed that the temperature jump parameter j, defined in Eq. (3.120), be used in all four regions to quantify conduction through a gas region, so that:

$$q_g'' = \frac{k_g}{d+j}(T_1 - T_2) \tag{5.13}$$

where q_g'' is the heat flux per unit area through the gas, d is the geometrical dimension of the gas-filled gap and k_g is the thermal conductivity of the gas. However, in the Multi-sphere Unit Cell Model each region is treated as unique in order to get a more accurate representation of the effective thermal conductivity when gas pressure varies. Thus, the following can be written for the interstitial gas in the middle region where the Smoluchowski effect is most likely to play a role:

$$Q_g = \int \frac{k_g 2\pi r (T_1 - T_2)}{D_{tot}(r) + j} dr \tag{5.14}$$

where $D_{tot}(r)$, is the total distance between the two spheres as a function of radius.

Slavin *et al.* (2002:4151) proposed using a polar angle to quantify the boundaries of this region. However, unlike other studies a newly derived mean free-path radius r_λ is used to indicate the limit of the Smoluchowski effect. This development is necessary because surface roughness in the Multi-sphere Unit Cell Model is not simplified using an average surface height h_r as in Slavin's *et al.* (2002:4151) case and more accurate integration boundaries are employed for the Smoluchowski effect. The thermal resistance of the interstitial gas in the middle region can be obtained by:

$$R_\lambda = \frac{1}{2\pi k_g}\left[\int_{r_a}^{r_\lambda} \frac{r}{D_{tot}(r)+j}dr\right]^{-1} \tag{5.15}$$

The mean free-path radius r_λ is developed by considering the equation for a circle with centre point (h,k):

$$r^2 = (x-h)^2 + (y-k)^2 \tag{5.16}$$

If the centre point is changed to $(0, r_p - \omega_0/2)$ with $r = r_p$, $x = r \geq r_a$ and $y = D(r)$, as graphically displayed in Figure 5.2, Eq. (5.16) can be rewritten to obtain $D(r)$ as:

$$D(r) = r_p - \frac{\omega_0}{2} - \sqrt{r_p^2 - r^2} \tag{5.17}$$

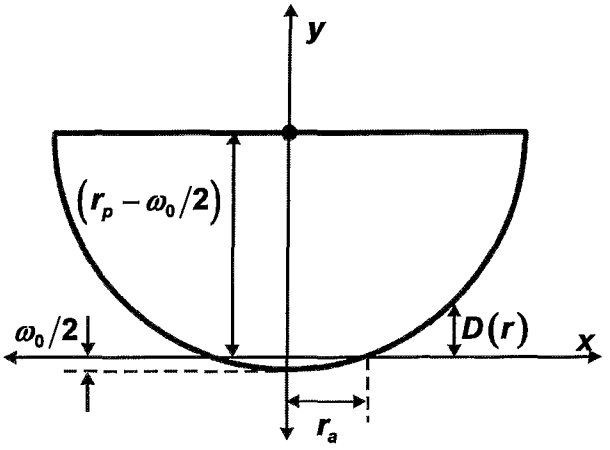

Figure 5.2: Interstitial gas conduction incorporating the Smoluchowski effect (middle region)[8]

Calculating the total distance between the two spheres as a function of radial position yields:

$$D_{tot}(r) = 2r_p - \omega_0 - 2\sqrt{r_p^2 - r^2} \tag{5.18}$$

Heat exchange exhibits a reduction in thermal conductivity when $1/Kn \leq 100$, as previously illustrated in Figure 3.2. However, if it is taken into consideration that the Smoluchowski effect only reduces thermal conductivity to a measurable extent when $1/Kn \leq 10$, then the following can be written:

$$\frac{1}{Kn} = \frac{d}{\lambda} = \frac{D_{tot}(r)}{\lambda} = 10 \tag{5.19}$$

so that $D_{tot}(r) = 10\lambda$. By substituting Eq. (5.19) into Eq. (5.18) and considering $r_\lambda = r$, the

[8] For the Hertzian contact network r_a changes to r_c.

mean free-path radius can be obtained by:

$$r_\lambda = \sqrt{r_p^2 - \left(r_p - 0.5\omega_0 - 5\lambda\right)^2} \tag{5.20}$$

where $r_a \le r_\lambda \le r_p$. Substituting Eq. (5.18) into Eq. (5.15) yields:

$$2\pi k_g R_\lambda = \left[\int_{r_a}^{r_\lambda} \frac{r}{2r_p - \omega_0 - 2\sqrt{r_p^2 - r^2} + j} dr\right]^{-1} \tag{5.21}$$

Integrating Eq. (5.21) leads to:

$$R_\lambda = \frac{2}{\pi k_g \left(A_\lambda \ln\left|\frac{A_\lambda - 2B_\lambda}{A_\lambda - 2C_\lambda}\right| + 2B_\lambda - 2C_\lambda\right)} \tag{5.22}$$

where $A_\lambda = 2r_p + j - \omega_0$, $B_\lambda = \sqrt{r_p^2 - r_\lambda^2}$, and $C_\lambda = \sqrt{r_p^2 - r_a^2}$. The full integration process is described in Appendix E.

The thermal resistance, $R_{mid,1,2}$ for the solid material in the range of $r_a \le r \le r_\lambda$ is developed by also assuming one-dimensional heat transfer. This is done on the same principle as for $R_{in,1,2}$. For both hemispheres of the unit cell, the thermal resistance for the middle solid region yields:

$$R_{mid,1,2} = 2\frac{\left(r_p - \omega_0/2\right)}{k_s\pi\left(r_\lambda^2 - r_a^2\right)} = \frac{\left(d_p - \omega_0\right)}{k_s\pi\left(r_\lambda^2 - r_a^2\right)} \tag{5.23}$$

Underlying the thermal resistance $R_{mid,1,2}$ is the fact that the conduction area remains the same over the total length of one hemisphere. The impact of this assumption on the effective thermal conductivity needs to be re-evaluated for very small diameter spheres because the region between the two limits could make up a large portion of the sphere. Nonetheless, the outer region conduction length is reduced to some extent, thereby reducing the outer solid thermal resistance as is explained later (Figure 5.3).

OUTER REGION CONDUCTION:

The same methodology employed to develop the interstitial gas thermal resistance R_λ is applied to develop the thermal conduction resistance R_G in the gas region $r_\lambda \le r \le r_p$. However, Eq. (5.14) is rewritten to accommodate the following problem as:

$$Q_G = \int \frac{k_g 2\pi r (T_1 - T_2)}{D_{tot}(r)} dr \tag{5.24}$$

Note that the temperature jump parameter j is neglected in Eq. (5.24) due to the fact that this gas region falls outside the bounds of the Smoluchowski effect. The thermal resistance of the interstitial gas in the outer region can be obtained by:

$$R_G = \frac{1}{2\pi k_g}\left[\int_{r_\lambda}^{r_p} \frac{r}{D_{tot}(r)} dr\right]^{-1} \tag{5.25}$$

Substituting Eq. (5.18) into Eq. (5.25) yields:

$$R_G = \frac{1}{2\pi k_g}\left[\int_{r_\lambda}^{r_p} \frac{r}{2r_p - \omega_0 - 2\sqrt{r_p^2 - r^2}} dr\right]^{-1} \tag{5.26}$$

After the integration, the following is obtained:

$$R_G = \frac{2}{\pi k_g \left(A_G \ln\left|\frac{A_G}{A_G - 2B_G}\right| - 2B_G\right)} \tag{5.27}$$

where $A_G = 2r_p - \omega_0$ and $B_G = \sqrt{r_p^2 - r_\lambda^2}$. The full integration process can be found in Appendix E.

For the development of the thermal resistance in the outer solid material region $R_{out,1,2}$, an isothermal temperature boundary is considered at the boundary of the sphere. This is a valid assumption owing to the high thermal conductivity of the matrix of a spherical graphite pebble. In addition, when heat is generated in the middle of the sphere, such as in the case of PBRs, the surface temperature will have a further tendency towards isothermal conditions.

For the derivation an orientation is assumed, where y is in the direction from the centre of the sphere under consideration towards the contact area, as displayed in Figure 5.3. Therefore, by considering this orientation the diametrical distance $d(y)$ can be obtained as a function of y, given by:

$$d(y) = 2\sqrt{r_p^2 - y^2} \tag{5.28}$$

The surface area for the desired outer solid conduction region yields:

$$A_c(y) = \frac{\pi}{4}\left(d(y)^2 - (2r_\lambda)^2\right) \tag{5.29}$$

Fourier's Law for one-dimensional conduction is used to derive a relation for the outer bulk solid thermal resistance, which is defined by:

$$Q_y = -k_s A_c \frac{\partial T}{\partial y} \tag{5.30}$$

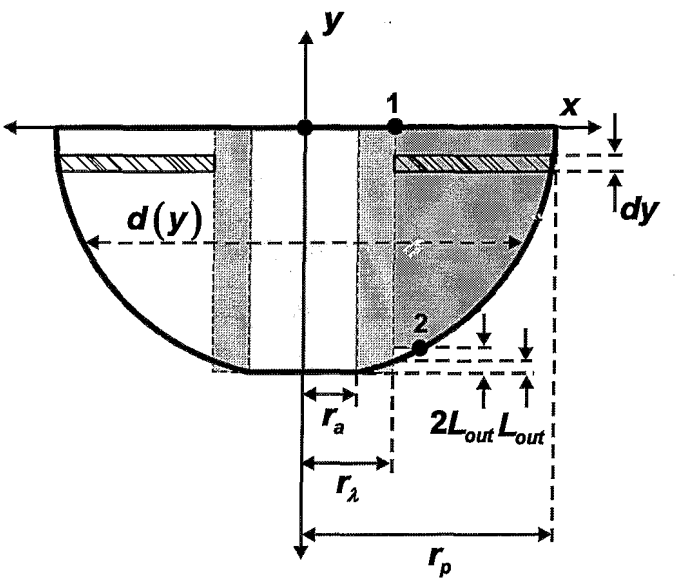

Figure 5.3: Pebble orientation for outer solid thermal resistance derivation[9]

Substituting Eq. (5.28) and Eq. (5.29) into Eq. (5.30), the thermal resistance yields:

$$\frac{Q_y}{k_s \pi} \int_0^{r_p - 2L_{out}} \frac{1}{\left(r_p^2 - r_\lambda^2 - y^2\right)} \partial y = -\int_{T_2}^{T_1} \partial T \tag{5.31}$$

where $L_{out} = \left(0.5\omega_0 + 5\lambda\right)$. T_1 is the temperature in the centre plane of the pebble and T_2 the temperature at a distance $2L_{out}$ from the contact surface, as displayed in Figure 5.3.

It must be emphasised that the total bulk region thermal resistance (inner, middle and outer) could have been derived using only one integration step (thermal resistance parameter). However, it is done in the fashion discussed in particular to illustrate the simplicity of adding thermal resistances, representing different thermal conductivities in a fuel matrix.

After the integration process the thermal resistance in the outer bulk region for both spheres in the unit cell where $r_p > r_\lambda$ can be obtained from:

[9] For the Hertzian contact network r_a changes to r_c.

$$R_{out,1,2} = \frac{\ln\left|\frac{A_{out}+B_{out}}{A_{out}-B_{out}}\right|}{k_s \pi B_{out}} \tag{5.32}$$

where $A_{out} = r_p - 2\left(0.5\omega_0 + 5\lambda\right)$, $B_{out} = \sqrt{r_p^2 - r_\lambda^2}$ and r_λ is the mean free-path radius defined in Eq. (5.20). The full integration process can be found in Appendix E.

Combining the different aforementioned parallel and series thermal resistances leads to an overall joint resistance R_j, obtained in Eq. (5.3) or Eq. (5.4). Calculating the effective thermal conductivity vector $\vec{k}_e^{g,c}$ through two spheres using R_j yields:

$$\vec{k}_e^{g,c} = \frac{L_j}{R_j A_j} = \frac{\left(d_p - \omega_0\right)}{d_p^2 R_j} \tag{5.33}$$

where $L_j = \left(d_p - \omega_0\right)$ and $A_j = d_p^2$ is the joint conduction area for any two half-spheres in contact with each other within in a packed bed. Although the Multi-sphere Unit Cell Model is essentially a cylindrical control volume, the heat transfer must be normalised by the effective square/rectangular area/control volume into which the cylinder fits because the integration in the application of the effective conductivity is performed over the entire cylindrical surface.

In order to obtain the radial heat transfer only and to account for the porous structure in a randomly packed bed, the radial component of the effective conductivity vector with the appropriate local averaged contact angle $\bar{\phi}_c$ needs to be calculated, multiplied by the average coordination flux number $\bar{n} = \bar{N}_c/2$ to account for the actual number of spheres in contact in a specific region. This which leads to:

$$k_e^{g,c} = \frac{\bar{N}_c\left(d_p - \omega_0\right)}{2 d_p^2 R_j} \sin\bar{\phi}_c \tag{5.34}$$

where $\bar{\phi}_c$ is in degrees and can be obtained from Eq. (2.27) and the coordination number $\bar{N}_c$ can be obtained from Eq. (2.22).

5.1.2 RADIATION

Yavanovich & Marotta (2006:261) noted that thermal radiation heat transfer inside the microgaps $0 \le r \le r_a$ is complex and very difficult to characterise. Bahrami *et al.* (2004:226) in contrast derived a ratio between the radiative conductivity and thermal conductance

through the contact area between a flat and a spherical surface. They demonstrated that although radiation through the contact area becomes relatively important at higher temperatures, the radiation heat transfer contribution is still far less than that of the conductance. Therefore, in this study it is considered that the dominant area of thermal radiation heat transfer occurs in the region between $r_a \le r \le r_p$ for the rough contact network or $r_c \le r \le r_p$ for the Hertzian contact network.

Equation (3.129) demonstrated the method most often employed to calculate the contribution of radiative heat transfer through a randomly packed bed. It is important to note that the radiation exchange factor F_E^* is generally calculated for the entire porous structure spectrum. However, in this study radiation exchange is quantified between two full spheres individually and not for the entire porous structure.

Furthermore, the effective conductivity due to radiation (denoted as radiative conductivity) developed in this study consists of two components: radiation exchange between spheres in contact (short-range radiation) and radiation exchange through voids from spheres not touching the sphere under consideration (long-range radiation), so that:

$$k_e^r = k_e^{r,S} + k_e^{r,L} \tag{5.35}$$

SHORT-RANGE THERMAL RADIATION:

A parameter for short-range thermal radiation is developed by considering standard radiative heat transfer between two gray diffuse parallel plates, given by:

$$Q_r = \frac{\sigma\left(T_1^4 - T_2^4\right)}{\left(\frac{1-\varepsilon_{r,1}}{\varepsilon_{r,1}A_1}\right) + \frac{1}{A_1 F_{1-2}} + \left(\frac{1-\varepsilon_{r,2}}{\varepsilon_{r,2}A_2}\right)} \tag{5.36}$$

where $\sigma = 5.67\times10^{-8}\left[W/m^2K^4\right]$ is the Stephan–Boltzmann constant for radiation F_{1-2} the radiation view factor, and, T_j , A_j , $\varepsilon_{r,j}$ are the temperature, heat transfer area and solid emissivity of the *j*-th plates (spheres), respectively. By considering that $\varepsilon_{r,1} = \varepsilon_{r,2} = \varepsilon_r$ and $A_{j,1} = A_{j,2} = A_s$, Eq. (5.36) can be rewritten as follows:

$$Q_r = \frac{A_s\sigma\left(T_1^4 - T_2^4\right)}{\left(\frac{2-2\varepsilon_r}{\varepsilon_r} + \frac{1}{F_{1-2}}\right)} \tag{5.37}$$

where $A_s = 4\pi r_p^2$, i.e. the surface area of a full sphere. The diffuse view factor between two

touching hemispheres (half spheres) is given by Wakao *et al.* (1969:118) as:

$$F_{1-2} = 0.1511 \tag{5.38}$$

It is important to note that Eq. (5.38) is based on the surface area of $A_s = 2\pi r_p^2$, i.e. a half sphere, and therefore the view factor based on the area of a full sphere in Eq. (5.37) will be:

$$F_{1-2} = 0.0756 \tag{5.39}$$

due to the reciprocity rule $A_i F_{i-j} = A_j F_{j-i}$. The radiative conductivity is considered to be:

$$k_e^{r,S} = \frac{Q_r L_r}{A_r (T_1 - T_2)} \tag{5.40}$$

where $L_r = d_p$ is a geometrical length characterising radiative conductivity. Radiative conductivity is also normalised with the same area as that for conduction in Eq. (5.33), i.e. $A_r = A_j = d_p^2$. For $\Delta T/\overline{T} << 1$, the following approximation is valid:

$$\frac{\left(T_1^4 - T_2^4\right)}{\left(T_1 - T_2\right)} \approx 4\overline{T}^3 \tag{5.41}$$

By substituting Eq. (5.40) and Eq. (5.41) into Eq. (5.37), the radiative conductivity vector $\vec{k}_e^r$ is obtained as:

$$\vec{k}_e^{r,S} = \frac{4 d_p \sigma A_s \overline{T}^3}{A_r \left(\frac{2 - 2\varepsilon_r}{\varepsilon_r} + \frac{1}{F_{1-2}} \right)} \tag{5.42}$$

The radial component of the vector is employed using the same methodology as that for $k_e^{g,c}$, by incorporating the average contact angle $\overline{\phi}_c$ and multiplying with the average coordination flux number $\overline{n} = \overline{N}_c/2$ to give:

$$k_e^{r,S} = \frac{2\overline{N}_c d_p \sigma A_s \overline{T}^3}{A_r \left(\frac{2 - 2\varepsilon_r}{\varepsilon_r} + \frac{1}{F_{1-2}} \right)} f_k \sin\overline{\phi}_c \tag{5.43}$$

where f_k is the non-isothermal correction factor explained later in Section 5.3, $\overline{\phi}_c$ can be obtained from Eq. (2.27) and the coordination number $\overline{N}_c$ can be obtained from Eq. (2.22).

LONG-RANGE THERMAL RADIATION:

Long-range thermal radiation is a complex phenomenon, due to the difficulty in characterising

the porous structure. This phenomenon can be defined as thermal radiation between spheres not in contact with each other, through the void spaces in the packing arrangement. Vortmeyer (1978:525) argued that unit cell models have never taken into account the long-range effects that must exist in packed beds.

However, in the Multi-sphere Unit Cell Model particular attention is given to long-range thermal radiation in the form of an average long-range diffuse view factor. That said, attention is only given to the bulk region of the packed bed in quantifying long-range radiation due to the complexity in characterising the average long-range diffuse view factor in the near-wall region. This is complex because at each particular distance from a reflector wall in the near-wall region the average view factor will differ until the bulk region is reached where it will be constant. For that reason, in this study, the contribution of long-range radiation to the effective thermal conductivity is assumed to be the same in the near-wall region as in the bulk region.

Now consider the long-range diffuse view factor F_{1-2}^{L} which decreases when the geometrical length L_r increases, where $F_{1-2} = 0.0756$ when $L_r = d_p$ or $z = 1$ (two touching spheres). It is expected that the function will look like that displayed in Figure 5.4. Therefore, it can be stated that:

$$\lim_{L_r \to z} F_{1-2}^{L}(L_r) = 0 \tag{5.44}$$

where L_r is the distance between the centre of the sphere under consideration and the centre of the long-range sphere and z in this case is the number of sphere diameters it will take to result in a long-range diffuse view factor of zero.

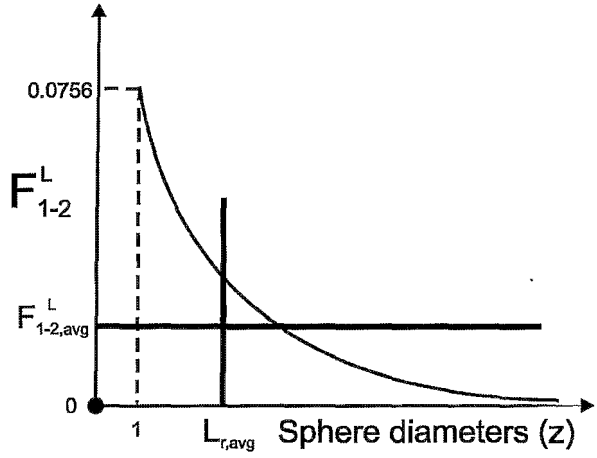

Figure 5.4: Decreasing long-range diffuse view factor in the bulk region based on surface area of a full sphere

Pitso (2009) investigated the decrease in $F_{1-2}^{L} = f(L_r)$ by using coordinates in the bulk region of a numerically generated packed bed and calculating the view factors with a view factor calculator obtained in a CFD package. The result is displayed in Figure 5.5.

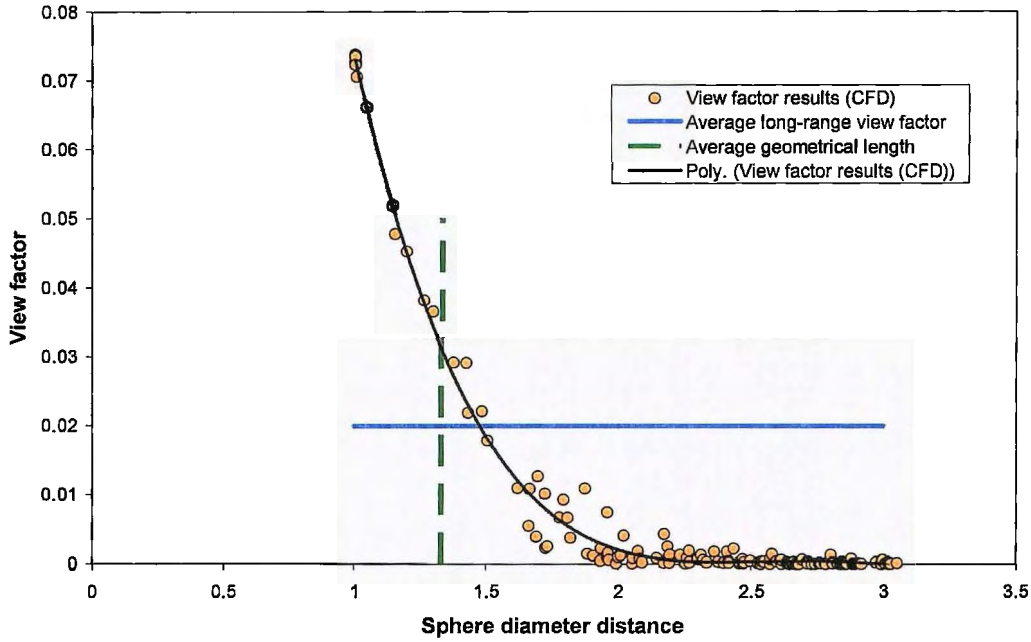

Figure 5.5: Long-range diffuse view factor in the bulk region (Pitso, 2009)

From Figure 5.5 it is evident that the number of sphere diameters it will take to decrease the long-range view factor to zero is in the vicinity of $z = 2.25$. Therefore, an average long-range diffuse view factor $F_{1-2,avg}^{L}$ can be obtained at an average geometrical length $L_{r,avg}$ by:

$$F_{1-2,avg}^{L} = \frac{\int_{1}^{2.25} F_{1-2}^{L}(L_r)\,dL_r}{1.25} \tag{5.45}$$

where $L_{r,avg}$ is obtained by:

$$L_{r,avg} = \frac{\int_{1}^{2.25} F_{1-2}^{L}(L_r)\,dL_r}{0.0756} + 1 \tag{5.46}$$

A polynomial curve was fitted through the data to obtain $F_{1-2}^{L} = f(L_r)$ and integrated as shown in Eq. (5.45) and Eq. (5.46). The result is that the average long-range diffuse view factor in the bulk region is:

$$F_{1-2,avg}^{L} = 0.0199 \tag{5.47}$$

and the average geometrical length:

$$L_{r,avg} = 1.33 d_p \tag{5.48}$$

Therefore, the radiative conductivity for the long-range thermal radiation in the bulk and near-wall regions is given by:

$$k_e^{r,L} = \frac{4L_{r,avg}\sigma A_s \bar{T}^3}{A_r\left(\frac{2-2\varepsilon_r}{\varepsilon_r}+\frac{1}{F^L_{1-2,avg}}\right)} f_k = \frac{4\left(1.33d_p\right)\sigma A_s \bar{T}^3}{A_r\left(\frac{2-2\varepsilon_r}{\varepsilon_r}+\frac{1}{F^L_{1-2,avg}}\right)} f_k \tag{5.49}$$

Underlying in Eq. (5.49) are the assumptions that $\Delta T/\bar{T} << 1$ for a distance of up to $z = 2.25$ and that the non-isothermal correction factor f_k stays the same for thermal radiation between surfaces further apart than $L_r = d_p$. Eq. (5.49) can then be rewritten to obtain:

$$k_e^{r,L} = \frac{\bar{n}_{long}\,5.32 d_p \sigma A_s \bar{T}^3}{A_r\left(\frac{2-2\varepsilon_r}{\varepsilon_r}+\frac{1}{F^L_{1-2,avg}}\right)} f_k \tag{5.50}$$

where $A_s = 4\pi r_p^2$ is the surface area of the sphere, $A_r = d_p^2$ is the radiative conduction area, $F^L_{1-2,avg}$ is the average long-range diffuse view factor, and $\bar{n}_{long}$ is the long-range coordination flux number representing the number of spheres that radiate long-range with the average view factor and length. This will be obtained empirically in Chapter 6. The approach presented here represents a first approximation to this complex phenomenon.

5.1.3 SPHERE – WALL CONDUCTION

In the case of the spheres in contact with the reflector wall a different model is required to characterise the heat transfer between the spheres and the reflector wall. The same approach followed in Section 5.1.1 is employed to develop $k_e^{g,c,W}$. However, the thermal resistance network was changed as displayed graphically in Figure 5.6.

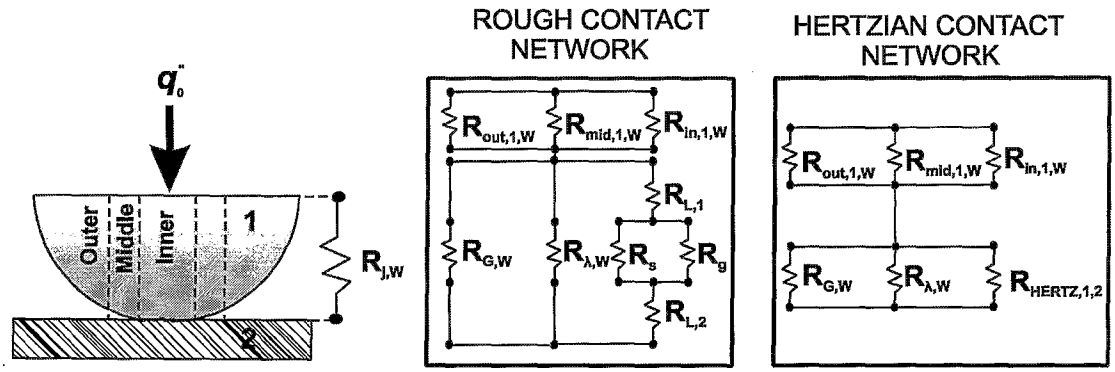

Figure 5.6: Multi-sphere Unit Cell Model (sphere–wall conduction)

The multi-sphere unit cell in the wall region consists of one-half sphere in contact with a flat wall. Again, the multi-sphere unit cell is divided into three radial regions (inner, middle and outer), and each of these regions consists of an arrangement of series and parallel resistances. However, the magnitude of certain of the thermal resistances is different from those in Section 5.1.1. The combined thermal resistance for the rough contact network between the half sphere and the flat wall is given by:

$$R_{j,W} = \left(\frac{1}{R_{L,1,2} + \left(\frac{1}{R_g} + \frac{1}{R_s} \right)^{-1}} + \frac{1}{R_{\lambda,W}} + \frac{1}{R_{G,W}} \right)^{-1} + \left(\frac{1}{R_{in,1,W}} + \frac{1}{R_{mid,1,W}} + \frac{1}{R_{out,1,W}} \right)^{-1} \quad (5.51)$$

where $R_{j,W}$ represents the total thermal resistance between the joint (half sphere and wall).

The combined thermal resistance for the Hertzian contact network is given by:

$$R_{j,W} = \left(\frac{1}{R_{HERTZ,1,2}} + \frac{1}{R_{\lambda,W}} + \frac{1}{R_{G,W}} \right)^{-1} + \left(\frac{1}{R_{in,1,W}} + \frac{1}{R_{mid,1,W}} + \frac{1}{R_{out,1,W}} \right)^{-1} \quad (5.52)$$

INNER REGION CONDUCTION:

The compact model to predict the thermal resistance through the microcontacts R_s for the wall region is given by:

$$R_s = \frac{0.565 H^* \left(\frac{\sigma_{RMS}}{m_{RMS}} \right)}{k_s^* F} \quad (5.53)$$

where the effective solid conductivity is $k_s^* = 2k_{s1}k_{s2}/(k_{s1} + k_{s2})$, if the thermal conductivity of two materials differs. R_g can be calculated with Eq. (5.7). For the macrocontact, the thermal resistance is given by:

$$R_{L,1,2} = \frac{1}{2k_s^* r_a} \quad (5.54)$$

where the contact area radius $r_a = a_L$ and can be obtained by Eq. (3.113). The Hertzian macrocontact resistance is given by:

$$R_{HERTZ,1,2} = \frac{0.64}{k_s^* r_c} \quad (5.55)$$

where r_c is calculated using Eq. (3.101).

In the wall region, only one sphere is considered. Therefore, the inner thermal resistance of the solid region for one hemisphere is:

$$R_{in,1,W} = \frac{\left(d_p - \omega_0\right)}{2k_s \pi r_a^2} \tag{5.56}$$

where k_s is the thermal conductivity of the solid material in the sphere, d_p is the sphere diameter, and the deformation depth $\omega_0 = r_a^2/2r_{p,eq}$. It must be emphasised that $r_{p,eq} = r_p$ in this setup. For the Hertzian contact network $R_{in,1,W}$ is defined in the same manner as displayed in Eq. (5.56), with the exeption of r_a changing to r_c which can be calculated with Eq. (3.101). This intuitively changes the deformation depth to $\omega_0 = r_c^2/2r_p$.

MIDDLE REGION CONDUCTION:

The heat transfer by conduction through the interstitial gas in-between the sphere and the wall is developed by changing the integration boundaries and the conduction length $D_W(r)$, so that Eq. (5.15) is rewritten as:

$$R_{\lambda,W} = \frac{1}{2\pi k_g}\left[\int_{r_a}^{r_{\lambda,W}} \frac{r}{D_W(r)+j}\,dr\right]^{-1} \tag{5.57}$$

where $r_{\lambda,W}$ is a new mean free-path radius for when $D_W(r) = 10\lambda$, with $D_W(r)$ given by:

$$D_W(r) = r_p - \omega_0 - \sqrt{r_p^2 - r^2} \tag{5.58}$$

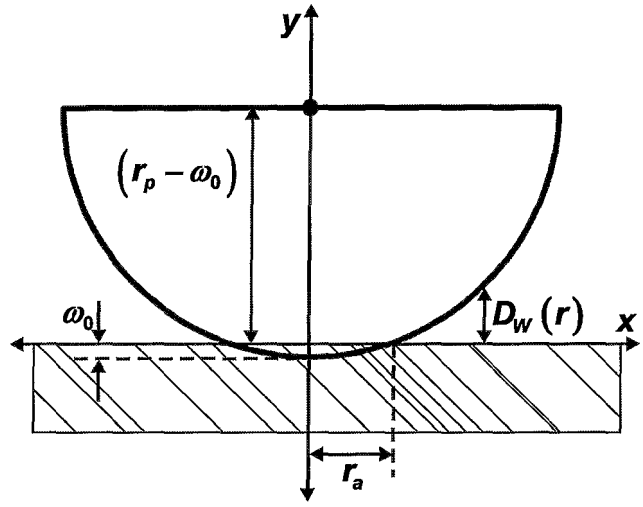

Figure 5.7: Interstitial gas conduction incorporating the Smoluchowski effect[10]

[10] For the Hertzian contact network r_a changes to r_c.

The mean free-path radius in the wall region can be obtained by considering $r_{\lambda,W} = r$, with Eq. (5.17) so that:

$$r_{\lambda,W} = \sqrt{r_p^2 - \left(r_p - \omega_0 - 10\lambda\right)^2} \tag{5.59}$$

where $r_a \le r_{\lambda,W} \le r_p$. Substituting Eq. (5.58) into Eq. (5.57) yields:

$$2\pi k_g R_{\lambda,W} = \left[\int_{r_a}^{r_{\lambda,W}} \frac{r}{r_p - \omega_0 - \sqrt{r_p^2 - r^2} + j} dr\right]^{-1} \tag{5.60}$$

After the integration, the following is obtained:

$$R_{\lambda,W} = \frac{1}{2\pi k_g \left(A_{\lambda,W} \ln\left|\frac{B_{\lambda,W} - A_{\lambda,W}}{C_{\lambda,W} - A_{\lambda,W}}\right| + B_{\lambda,W} - C_{\lambda,W}\right)} \tag{5.61}$$

where $A_{\lambda,W} = r_p + j - \omega_0$, $B_{\lambda,W} = \sqrt{r_p^2 - r_{\lambda,W}^2}$ and $C_{\lambda,W} = \sqrt{r_p^2 - r_a^2}$. The full integration process can be found in Appendix E.

For the thermal resistance in the solid middle region, Eq. (5.23) reduces to:

$$R_{mid,1} = \frac{\left(d_p - \omega_0\right)}{2k_s\pi\left(r_{\lambda,W}^2 - r_a^2\right)} \tag{5.62}$$

OUTER REGION CONDUCTION:

The thermal resistance of the heat transfer by conduction through the interstitial gas between $r_{\lambda,W} \le r \le r_p$ is given by:

$$R_{G,W} = \frac{1}{2\pi k_g}\left[\int_{r_{\lambda,W}}^{r_p} \frac{r}{D_W(r)} dr\right]^{-1} \tag{5.63}$$

where $D_W(r)$ is given by Eq. (5.58) and $r_{\lambda,W}$ is given by Eq. (5.59). Substituting Eq. (5.58) into Eq. (5.63) yields:

$$R_{G,W} = \frac{1}{2\pi k_g}\left[\int_{r_{\lambda,W}}^{r_p} \frac{r}{r_p - \omega_0 - \sqrt{r_p^2 - r^2}} dr\right]^{-1} \tag{5.64}$$

After the integration, the following is obtained:

$$R_{G,W} = \frac{1}{2\pi k_g \left(A_{G,W} \ln \left| \frac{A_{G,W}}{B_{G,W} - A_{G,W}} \right| - B_{G,W} \right)} \tag{5.65}$$

where $A_{G,W} = r_p - \omega_0$ and $B_{G,W} = \sqrt{r_p^2 - r_{\lambda,W}^2}$. The full integration process can be found in Appendix E.

The solid resistance in the outer bulk region is obtained using the same methodology as explained in Section 5.1.1 with the full integration process shown in Appendix E. However, due to the involvement of only one sphere in contact with the wall, the thermal resistance given in Eq. (5.32) reduces to:

$$R_{out,1,W} = \frac{\ln \left| \frac{A_{out,W} + B_{out,W}}{A_{out,W} - B_{out,W}} \right|}{2k_s \pi B_{out,W}} \tag{5.66}$$

where $A_{out,W} = r_p - 2(\omega_0 + 10\lambda)$ and $B_{out,W} = \sqrt{r_p^2 - r_{\lambda,W}^2}$. Calculating the effective thermal conductivity vector in the wall region $\vec{k}_e^{g,c,W}$, using the combined thermal resistance $R_{j,W}$, yields:

$$\vec{k}_e^{g,c,W} = \frac{L_{j,W}}{R_{j,W} A_{j,W}} = \frac{(r_p - \omega_0)}{d_p^2 R_{j,W}} \tag{5.67}$$

where $L_{j,W} = r_p - \omega_0$ and $A_{j,W} = d_p^2$. However, unlike Eq. (5.33), there is no need to account for the porous structure to obtain the radial component. Therefore, Eq. (5.67) is rewritten to give:

$$k_e^{g,c,W} = \frac{(r_p - \omega_0)}{d_p^2 R_{j,W}} \tag{5.68}$$

5.1.4 SPHERE–WALL AND WALL–SPHERE RADIATION

The thermal radiation in the wall region where $0 \le r \le 0.5 d_p$ is derived using the same methodology as described in Section 5.1.2. Thermal radiation is again divided into two components, namely the short-range thermal radiation and the long-range thermal radiation, so that:

$$k_e^{r,W} = k_e^{r,S,W} + k_e^{r,L,W} \tag{5.69}$$

SHORT-RANGE THERMAL RADIATION:

To calculate the short-range thermal radiation between a sphere and a reflector wall one must consider four variables i.e. surface area of sphere $A_1 = 4\pi r_p^2$, diffuse radiation view factor from a single sphere toward a reflector wall F_{1-2}^{W}, effective surface area of the wall A_2 and diffuse radiation view factor from the reflector wall towards the sphere F_{2-1}^{W}. Of the four variables only one is known i.e. A_1, and the procedure to calculate the other three is discussed below.

THERMAL RADIATION TO A WALL:

The diffuse radiation view factor F_{1-2}^{W} for thermal radiation between a sphere denoted as 1 and a coaxial disk denoted as 2 is given by Modest (1993:792) as:

$$F_{1-2}^{W} = \frac{1}{2}\left[1 - \frac{1}{\sqrt{1+\left(r_{disk}/a\right)^2}}\right] \tag{5.70}$$

where a is the distance between the centre of the sphere to the coaxial disk and r_{disk} is the radius of the disk. If one considers, $r_{disk} = \infty$ large and a is such that the sphere touches the disk, Eq. (5.70) becomes:

$$F_{1-2}^{W} = 0.5 \tag{5.71}$$

based on a radiating surface $A_s = 4\pi r_p^2$. However, one sphere does not interact with the wall alone. Therefore, due to other spheres also touching the wall the diffuse view factor towards the wall is restricted to some extent. Again the work of Pitso (2009) was used to obtain an accurate prediction of F_{1-2}^{W}. Pitso (2009) used a numerically generated packed bed situated at the outer wall (outer reflector) to obtain the view factor F_{1-2}^{W}. The outer wall has a larger circumference and therefore the curvature of the wall is not that large. A numerical view factor calculator was again used to obtain the view factor for the spheres touching the wall. The view factor was found to be:

$$F_{1-2}^{W} = 0.315 \tag{5.72}$$

Rewriting Eq. (5.40) for the wall region yields:

$$k_e^{r,S,W} = \frac{Q_r L_r^{W}}{A_r\left(T_1 - T_2\right)} \tag{5.73}$$

where T_1 is the temperature in the centre of the sphere, T_2 is the surface temperature on the

wall and $L_r^W = d_p/2$. Substituting Eq. (5.73) into Eq. (5.36), and neglecting the porous structure as with $k_e^{g,c,W}$, yields:

$$k_e^{r,S,W} = \frac{4\frac{d_p}{2}\sigma\bar{T}^3}{A_r\left[\left(\frac{1-\varepsilon_{r,1}}{\varepsilon_{r,1}A_1}\right)+\frac{1}{A_1F_{1-2}^W}+\left(\frac{1-\varepsilon_{r,2}}{\varepsilon_{r,2}A_2}\right)\right]}f_k = \frac{2d_p\sigma\bar{T}^3}{A_r\left[\left(\frac{1-\varepsilon_{r,1}}{\varepsilon_{r,1}A_1}\right)+\frac{1}{A_1F_{1-2}^W}+\left(\frac{1-\varepsilon_{r,2}}{\varepsilon_{r,2}A_2}\right)\right]}f_k \qquad (5.74)$$

where $A_r = d_p^2$, $A_1 = 4\pi r_p^2$ with f_k the non-isothermal correction factor explained later in Section 5.3, and F_{1-2}^W as presented in Eq. (5.72). From Eq. (5.74) one can observe that the remaining variable to be calculated is the effective surface area A_2 of the wall that exchanges heat with the sphere via radiation. This can be calculated via the reciprosity rule $A_1F_{1-2}^W = A_2F_{2-1}^W$. However, to achieve this one must first obtain the diffuse radiation view factor from the reflector wall towards the sphere F_{2-1}^W.

Furthermore, it must be emphasized, although not discussed yet, that the non-isothermal correction factor f_k between two spheres and between a sphere and a reflector wall is assumed in this study to be the same.

THERMAL RADIATION FROM A WALL:

The radiation view factor from a reflector surface to a sphere is different from that of a sphere towards a reflector surface due to the effective wall area A_2 being different. The diffuse view factor from the outer reflector wall towards the sphere was analysed by Pitso (2009) and found it to be:

$$F_{2-1}^W = 0.01976 \qquad (5.75)$$

Therefore, one can obtain the effective wall area A_2 by:

$$A_2 = \frac{A_1F_{1-2}^W}{F_{2-1}^W} = 63.77\pi r_p^2 \qquad (5.76)$$

LONG-RANGE THERMAL RADIATION:

The same methodology is followed to calculate the contribution of long-range thermal radiation to the effective thermal conductivity in the wall region as was done in the bulk region of a randomly packed bed.

THERMAL RADIATION TO A WALL:

The long-range diffuse view factor in the wall region $F_{1-2}^{L,W}$ is also assumed to decrease with an increasing geometrical length L_r^W, where $F_{1-2}^{L,W} = 0.315$ at $L_r^W = r_p = 0.5d_p$ or $z = 0.5$. Results generated by Pitso (2009) are displayed in Figure 5.8.

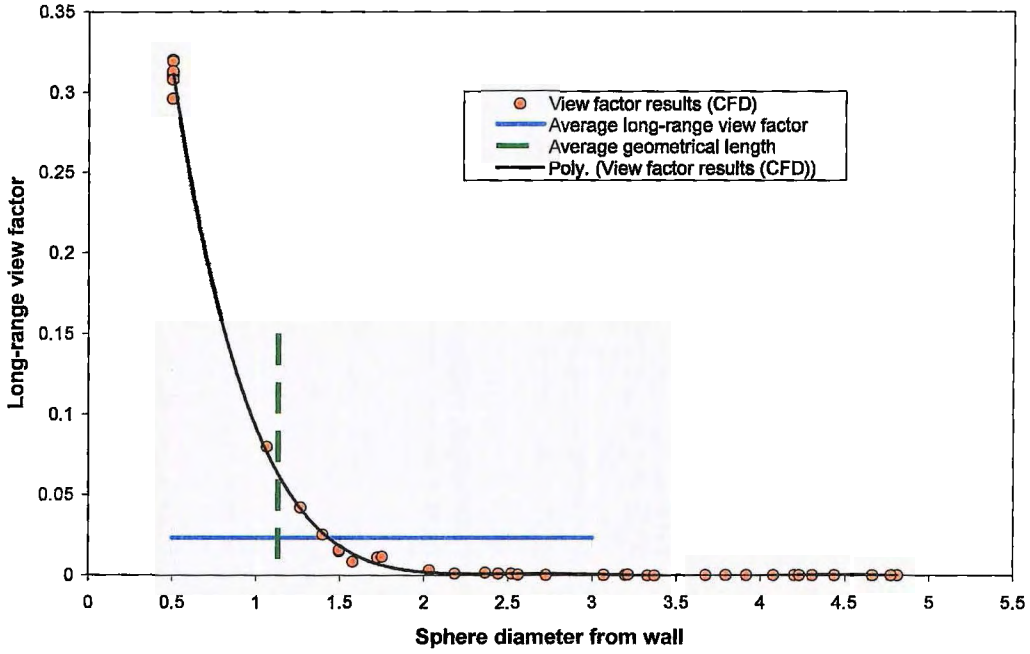

Figure 5.8: Long-range diffuse view factor for thermal radiation from spheres to the wall

It is important to note in Figure 5.8 that the first sphere not in contact with the wall is at a distance of $z = 1.065$ from the wall and that at a distance of $z = 2$ the long-range view factor goes to zero. Therefore, the integration boundaries are given by:

$$F_{1-2,avg}^{L,W} = \frac{\int_{1.065}^{2} F_{1-2}^{L,W}\left(L_r^W\right) dL_r^W}{0.935} \tag{5.77}$$

and the average geometrical length, $L_{r,avg}^W$, is obtained by:

$$L_{r,avg}^W = \frac{\int_{1.065}^{2} F_{1-2}^{L,W}\left(L_r^W\right) dL_r^W}{0.319} + 1.065 \tag{5.78}$$

The average long-range diffuse view factor for thermal radiation from spheres to the wall is therefore found to be:

$$F_{1-2,avg}^{L,W} = 0.02356 \tag{5.79}$$

and the average geometrical length is:

$$L_{r,avg}^{W} = 1.134 d_p \tag{5.80}$$

By following the same approach as that followed in the bulk region, Eq. (5.49) can be rewritten to obtain:

$$\begin{aligned} k_e^{r,L,W} &= \frac{\bar{n}_{long}^{W} 4\left(1.134 d_p\right)\sigma \bar{T}^3}{A_r\left[\left(\frac{1-\varepsilon_{r,1}}{\varepsilon_{r,1}A_1}\right)+\frac{1}{A_1 F_{1-2,avg}^{L,W}}+\left(\frac{1-\varepsilon_{r,2}}{\varepsilon_{r,2}A_2}\right)\right]} f_k \\ &= \frac{\bar{n}_{long}^{W} 4.536 d_p \sigma \bar{T}^3}{A_r\left[\left(\frac{1-\varepsilon_{r,1}}{\varepsilon_{r,1}A_1}\right)+\frac{1}{A_1 F_{1-2,avg}^{L,W}}+\left(\frac{1-\varepsilon_{r,2}}{\varepsilon_{r,2}A_2}\right)\right]} f_k \end{aligned} \tag{5.81}$$

where $A_r = d_p^2$, $A_1 = 4\pi r_p^2$, f_k the non-isothermal correction factor explained later in Section 5.3, $F_{1-2,avg}^{L,W}$ as presented in Eq. (5.79), with 1 representing the long-range sphere and 2 representing the wall and $\bar{n}_{long}^{W}$ the long-range coordination flux number in the wall region, representing the number of spheres radiating to the wall with the average view factor and length. The long-range coordination flux number is obtained empirically in Chapter 6. Just as in the case of short-range radiation is the remaining variable in Eq. (5.81) A_2. This can again be calculated via the reciprocity rule.

THERMAL RADIATION FROM A WALL:

As with $F_{1-2}^{L,W}$, is it found that $F_{2-1}^{L,W}$ decreases with increasing geometrical length L_r^W, where $F_{2-1}^{L,W} = 0.01976$ when $L_r^W = r_p = 0.5 d_p$ or $z = 0.5$ (Figure 5.9). The average long-range view factor $F_{2-1,avg}^{L,W}$ was obtained using the same method as presented in Figure 5.8. After integrating, the average long-range diffuse view factor for thermal radiation from the wall to the spheres is found to be:

$$F_{2-1,avg}^{L,W} = 0.00148 \tag{5.82}$$

with the average geometrical length $L_{r,avg}^{W} = 1.134 d_p$. Using the reciprocity rule, the effective flat surface area can be obtained by:

$$A_2 = \frac{A_1 F_{1-2}^{L,W}}{F_{2-1}^{L,W}} = 63.68\pi r_p^2 \tag{5.83}$$

The results obtained in Eq. (5.76) and Eq. (5.83) is almost exactly the same. It was decided to take $A_2 = 63.68\pi r_p^2$ in this study for both short and long-range radiation in the wall region.

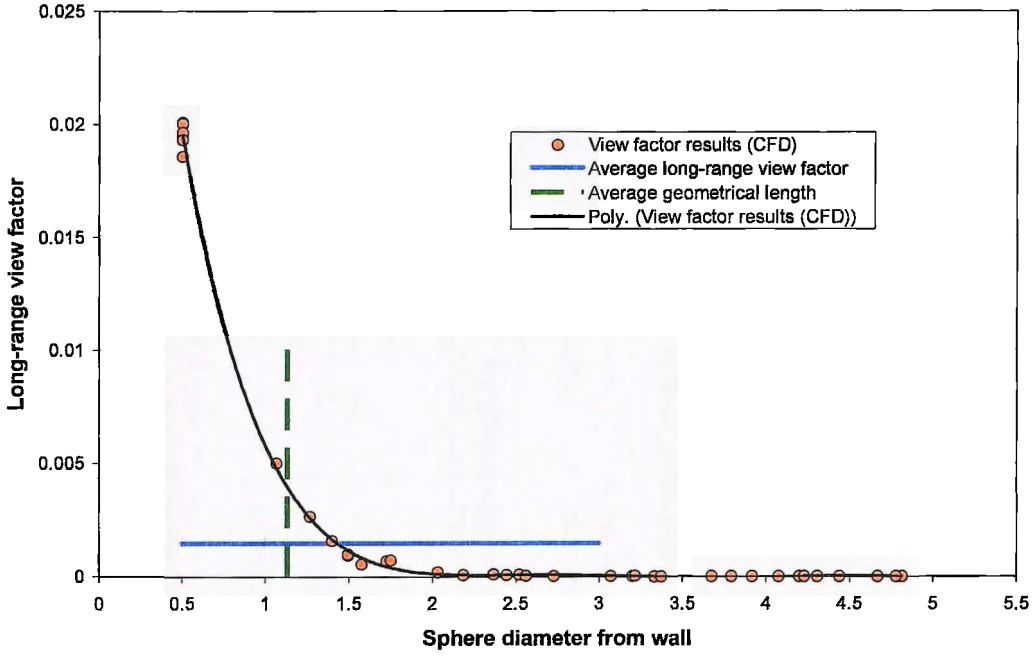

Figure 5.9: Long-range diffuse view factor for thermal radiation from wall to spheres

5.3 THE EFFECT OF SOLID CONDUCTIVITY ON THERMAL RADIATION

A decrease in thermal conductivity in the solid material not only influences heat transfer by reducing the conductivity through two spheres in contact, but also influences the thermal radiation heat transfer between the two spherical surfaces. This is noted by Singh & Kaviany (1994:2579), who demonstrated that the radiant conductivity k_e^r is strongly influenced by the solid conductivity k_s and pebble emissivity ε_r, and introduced a dimensionless solid conductivity $\Lambda_s = k_s/4d_p\sigma T^3$ parameter as explained in Eq. (3.129).

The reason for this is that the isothermal surface temperature assumption is no longer valid and large temperature gradients may arise on the surfaces of the spheres as the solid conductivity k_s decreases. This results in a lower surface temperature at the tip of the sphere, implying a decrease in thermal radiative exchange at that point. Therefore, this approach is also adopted in this study.

For the Multi-sphere Unit Cell Model the effect of solid conductivity on thermal radiation was investigated using a numerical simulation of radiation heat transfer between two hemispheres

of $d_p = 60mm$, separated by a distance of $0.5mm$, eliminating any chances of heat transfer by conduction. The numerical calculations were conducted using a CFD package (STAR-CCM+).

The thermal radiation between two hemispheres was investigated using the parameters displayed in Figure 5.10 and varying the solid conductivity from high to low. The full procedure and data can be found in Appendix F.

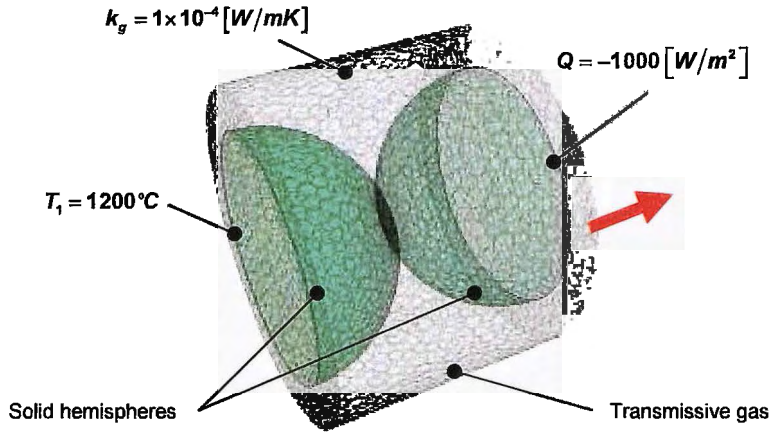

Figure 5.10: Thermal radiation heat transfer between two hemispheres

Based on the results of the numerical simulation, the normalised non-isothermal correction factor f_k, displayed in Figure 5.11, is proposed to address the decrease in radiative conductivity k_e^r, with a decrease in k_s. The non-isothermal correction factor is also given by:

$$f_k = a_1 \tan^{-1}\left(a_2\left(\frac{1}{\Lambda_s}\right)^{a_3}\right) + a_4 \tag{5.84}$$

where $\Lambda_s = k_s/4d_p\sigma T^3$ and $f_k = 1$ when $1/\Lambda_s < 0.01$. The empirical constants are valid for $0.2 \le \varepsilon_r \le 1$ and for $0.01 \le 1/\Lambda_s \le 10$ and can be obtained by:

$$a_1 = 0.0841\varepsilon_r^2 - 0.307\varepsilon_r - 0.1737 \tag{5.85}$$

$$a_2 = 0.6094\varepsilon_r + 0.1401 \tag{5.86}$$

$$a_3 = 0.5738\varepsilon_r^{-0.2755} \tag{5.87}$$

$$a_4 = 0.0835\varepsilon_r^2 - 0.0368\varepsilon_r + 1.0017 \tag{5.88}$$

It must be emphasised that the function presented above is only valid for the given dimensionless solid conductivity range and should be re-evaluated if used out of the limits

specified for $1/\Lambda_s$. In addition, it must also be emphasised that Figure 5.11 was developed for spheres in close proximity, implying a correction factor for short-range radiation. Further research needs to be conducted regarding the evaluation of the difference between the non-isothermal correction factor for short-range and long-range radiation. For this study, the non-isothermal correction factors for short-range and long-range radiation are assumed to be the same.

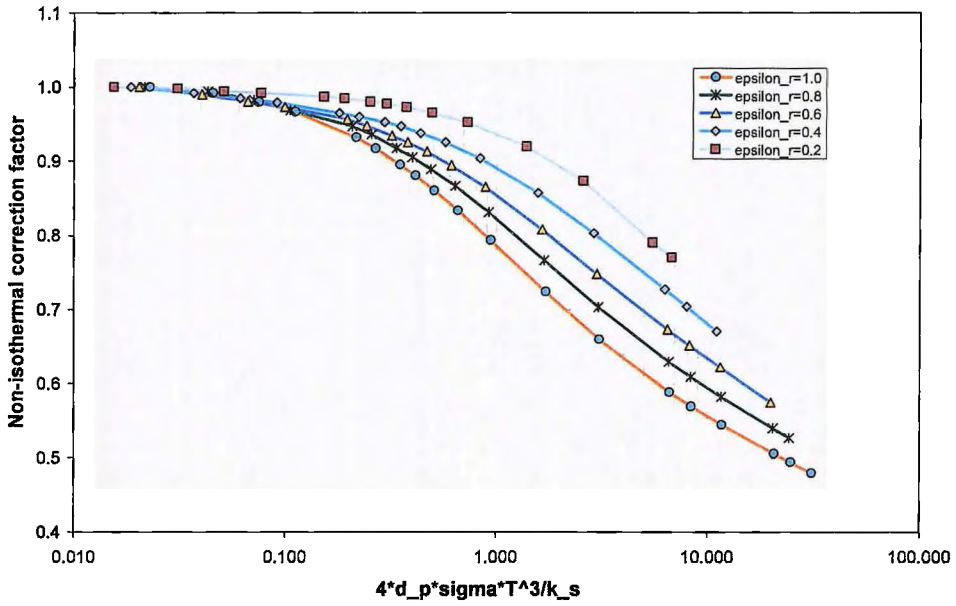

Figure 5.11: Non-isothermal correction factor (derived in Appendix F)

Note that a similar concept is also implemented in the Breitbach & Barthels (1980:392) correlation, Eq. (3.150), and is given by:

$$f_k^{BB} = \frac{1}{1+\frac{1}{\left(\frac{2}{\varepsilon_r}-1\right)\Lambda_s}} \tag{5.89}$$

The same graph was generated using Eq. (5.89) as done for Figure 5.11, with results displayed in Appendix F (see Figure F.3). It demonstrates that the non-isothermal correction factor declines much faster than what is given in Figure 5.11. One possible reason may be that Breitbach & Barthels (1980:392) derived an equation addressing thermal radiation in a randomly packed bed as a whole and did not attempt to separate short and long-range thermal radiation.

5.4 CONCLUSION

This chapter presented the derivation of the Multi-sphere Unit Cell Model. Two different sets of equations were developed, one for the calculation of effective thermal conductivity in the bulk region which inherently can also calculate the effective thermal conductivity in the near-wall region, as well as a second set to calculate the effective thermal conductivity in the wall region.

Furthermore, an effective long-range diffuse view factor was proposed for the bulk region, as well as for the wall region. The only parameters that remains to be addressed are $\bar{n}_{long}$ and $\bar{n}^{W}_{long}$, the long-range coordination flux numbers for the bulk and wall regions. These parameters are obtained empirically from the comparison between the Multi-sphere Unit Cell Model and the experimental data that is presented in Chapter 6.